



**HAL**  
open science

# Chromato-axial memory effect in step index multimode fibers

Louisiane Devaud, Marc Guillon, Ivan Gusachenko, Sylvain Gigan

► **To cite this version:**

Louisiane Devaud, Marc Guillon, Ivan Gusachenko, Sylvain Gigan. Chromato-axial memory effect in step index multimode fibers. *APL Photonics*, 2021, 6 (12), pp.126105. 10.1063/5.0067892. hal-03512066

**HAL Id: hal-03512066**

<https://hal.sorbonne-universite.fr/hal-03512066v1>

Submitted on 5 Jan 2022

**HAL** is a multi-disciplinary open access archive for the deposit and dissemination of scientific research documents, whether they are published or not. The documents may come from teaching and research institutions in France or abroad, or from public or private research centers.

L'archive ouverte pluridisciplinaire **HAL**, est destinée au dépôt et à la diffusion de documents scientifiques de niveau recherche, publiés ou non, émanant des établissements d'enseignement et de recherche français ou étrangers, des laboratoires publics ou privés.

# Chromato-axial memory effect in step-index multimode fibers

Cite as: APL Photonics **6**, 126105 (2021); <https://doi.org/10.1063/5.0067892>

Submitted: 20 August 2021 • Accepted: 22 November 2021 • Accepted Manuscript Online: 23 November 2021 • Published Online: 08 December 2021

 Louisiane Devaud,  Marc Guillon,  Ivan Gusachenko, et al.



View Online



Export Citation



CrossMark

## ARTICLES YOU MAY BE INTERESTED IN

[Observing distant objects with a multimode fiber-based holographic endoscope](#)

APL Photonics **6**, 036112 (2021); <https://doi.org/10.1063/5.0038367>

[Higher-order exceptional point and Landau-Zener Bloch oscillations in driven non-Hermitian photonic Lieb lattices](#)

APL Photonics **6**, 126106 (2021); <https://doi.org/10.1063/5.0069633>

[Giant chiroptical response of twisted metal nanorods due to strong plasmon coupling](#)

APL Photonics **6**, 126104 (2021); <https://doi.org/10.1063/5.0069371>



APL Photonics

2020 Future **Luminary** Collection

READ NOW

# Chromato-axial memory effect in step-index multimode fibers

Cite as: APL Photon. 6, 126105 (2021); doi: 10.1063/5.0067892  
Submitted: 20 August 2021 • Accepted: 22 November 2021 •  
Published Online: 8 December 2021



View Online



Export Citation



CrossMark

Louisiane Devaud,<sup>1,a)</sup>  Marc Guillon,<sup>2</sup>  Ivan Gusachenko,<sup>1</sup>  and Sylvain Gigan<sup>1</sup> 

## AFFILIATIONS

<sup>1</sup>Laboratoire Kastler Brossel, CNRS, Collège de France, ENS-Université PSL, Sorbonne Université, 24 rue Lhomond, 75005 Paris, France

<sup>2</sup>Saints-Pères Paris Institute for the Neurosciences, CNRS UMR 8003, Université de Paris, 45 rue des Saints-Pères, Paris 75006, France

<sup>a)</sup> Author to whom correspondence should be addressed: [louisiane.devaud@lkb.ens.fr](mailto:louisiane.devaud@lkb.ens.fr)

## ABSTRACT

Multimode fibers (MMFs) are used in many applications from telecommunications to minimally invasive micro-endoscopic imaging. However, the numerous modes and their coupling make light-beam control and imaging a delicate task. To circumvent this difficulty, recent methods exploit priors about the transmission of the system, such as the so-called optical memory effect. In this paper, we quantitatively characterize a chromato-axial memory effect in step-index MMFs, characterized through its slope  $\delta z/\delta\lambda$  and its spectral and axial widths. We propose a theoretical model and numerical simulations that are in good agreement with experimental observations.

© 2021 Author(s). All article content, except where otherwise noted, is licensed under a Creative Commons Attribution (CC BY) license (<http://creativecommons.org/licenses/by/4.0/>). <https://doi.org/10.1063/5.0067892>

## I. INTRODUCTION

Multimode fibers (MMFs) are ubiquitous tools having a key role in telecommunications<sup>1</sup> and driving research in many other related fields, such as MMF lasers,<sup>2</sup> fiber-based tunable optical cavities,<sup>3</sup> and reconfigurable linear operators in quantum photonics applications.<sup>4,5</sup> MMFs have also been shown to be useful as high-resolution spectrometers.<sup>6,7</sup> In addition, MMFs have recently raised much hope for developing non-invasive imaging techniques and minimally invasive endoscopes.<sup>8,9</sup> Due to the complex nature of multimode guided propagation, light-field control through MMFs has highly benefited from recent progress in wavefront shaping techniques, initially developed for adaptive optics in astronomy<sup>10,11</sup> and then extended to complex media.<sup>12</sup> As for propagation through complex media, uncontrolled coherent light propagation through a MMF results in a speckle intensity pattern.<sup>13,14</sup> Light-field control at the distal tip of the fiber demands iterative optimization<sup>15</sup> or transmission matrix (TM) measurement.<sup>12,16</sup> Not only is this calibration experimentally delicate, but it is also very sensitive to perturbations, such as mechanical or thermal fluctuations. In this regard, significant progress has been made for controlling short MMF eigenmodes, resulting, in particular, in an increased robustness to bending.<sup>17,18</sup> New strategies have also been developed to help

TM measurement using continuous optimization<sup>19</sup> or exploiting priors.<sup>20</sup>

A major prior information about the TM of complex media is the so-called “optical memory effect” (ME), referring to optical-field transforms that commute with the TM or, equivalently, those that are diagonal in the eigen-basis of the TM.<sup>20</sup> The expression ME has been coined in the context of scattering media where for a thin enough diffuser, wavefront tilting has been demonstrated, both theoretically<sup>21</sup> and experimentally,<sup>22</sup> to be preserved along the propagation. This spatial ME has then been extended to scattering media with strong anisotropy factors.<sup>23,24</sup> Based on the cylindrical symmetry of MMFs, the rotational ME could be demonstrated.<sup>25,26</sup> Recently, the concept of ME has even been broadened to the spectral domain.<sup>27,28</sup> It has been shown experimentally that a chromatic shift induces an axial drift of a beam focused by wavefront shaping behind 1 mm-thick brain tissues, over spectral widths as large as  $\sim 100$  nm.<sup>27</sup> Theoretical modeling established that this broadband chromato-axial ( $\chi$ -axial) ME is a characteristic of forward scattering media thinner than the transport mean free path,<sup>28</sup> where the product  $\lambda z$  (wavelength and axial plane) is specifically conserved when illuminated by a plane wave.<sup>28,29</sup> In essence, the  $\chi$ -axial ME is due to the conservation of the transverse component of the wave-vector under spectral detuning. Interestingly, this

conservation naturally holds in step-index (SI) MMFs.<sup>16</sup> Furthermore, broadband light propagation through a MMF has recently been observed resulting in an axially extended focus, allowing efficient volumetric imaging.<sup>30,31</sup> In this article, we experimentally characterize the  $\chi$ -axial ME, so far unexplored, at the distal facets of SI-MMFs and theoretically model it based on the study of the correlation function. The two eigen-axes of the correlation function, diagonal wherein the TM of the MMFs, are analytically derived, together with their respective widths.

## II. EXPERIMENTAL SETUP, OBSERVATION, AND INTERPRETATION

### A. Experimental description

As illustrated in Fig. 1(a), our experiment consists of a tunable Ti:sapphire laser emitting a linearly polarized monochromatic light coupled to a SI-MMF with a microscope objective. In all experiments, MMFs of 0.22 numerical aperture (NA) and lengths  $L = 29, 58, \text{ and } 120 \text{ mm}$  are tightly held straight. The objectives' NA (0.25) is chosen to be slightly larger than that of the fibers to ensure that light is well coupled to all fiber modes. At the MMF output, an objective lens mounted on an axial-translation stage collects the light and sends it to a CCD camera through a tube lens. This arrangement enables the imaging of different axial planes  $z$  at the MMF output while tuning the wavelength [see Fig. 1(b)]. The input wavefront can be controlled by a spatial light modulator (SLM) conjugated with the back focal plane of the input objective in order to either refocus the beam after the MMF or generate random input fields.

In a first set of experiments, we engineered a focused 800 nm laser spot just after the MMF by input wavefront modulation using the TM of the fiber. The TM is measured by sequentially displaying a basis of modes onto the SLM and gradually phase stepping them.<sup>12</sup> The focus is then generated by phase conjugation. When applying a spectral shift to the input beam, the focus is observed to be axially shifted at the MMF output [Fig. 1(c)], similar to what was observed through forward scattering media.<sup>27</sup> The  $\chi$ -axial ME is observed not only for an engineered focused spot but also when coupling random light patterns to the fiber. In this case, the similarity of speckles can be observed by computing the zero-mean cross-correlation products between output speckles,<sup>28</sup>

$$C(\delta z, \delta \lambda) = \frac{\langle \tilde{I}(\delta z, \delta \lambda) \tilde{I}_0 \rangle}{\sqrt{\langle \tilde{I}^2(\delta z, \delta \lambda) \rangle \langle \tilde{I}_0^2 \rangle}} \quad (1)$$

with  $\tilde{I} = I - \langle I \rangle$ , where  $\langle \rangle$  stands for spatial averaging over all speckle grains. The 0 index represents the reference speckle image at  $z = 0$  and  $\lambda_0 = 800 \text{ nm}$ , to which all the other ones are compared. Importantly, before computing the correlation product of experimental images, we numerically corrected them from potential transverse drifts and intensity inhomogeneities (see the [supplementary material](#)). The correlation products of the so-corrected experimental intensity patterns are shown in Fig. 1(d) as a function of  $\delta z$  and  $\delta \lambda$ .

Similar to what we obtain for the focused spot, a  $\chi$ -axial ME is obtained for output speckles: a correlation line appears when comparing speckles, proving the coupling between  $\lambda$  and  $z$  shifts. In

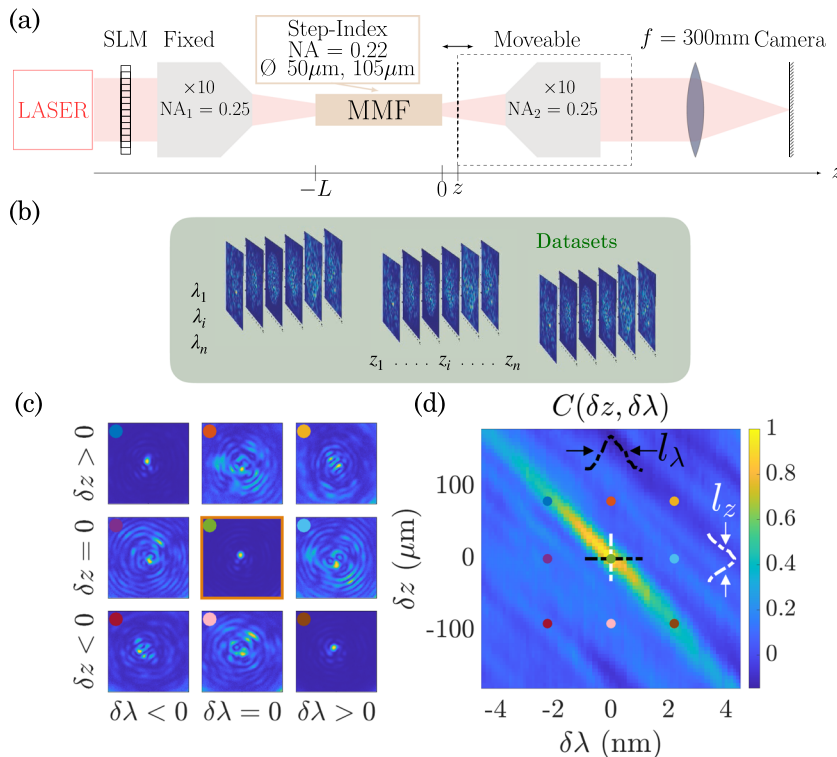


**FIG. 1.** Experimental setup and procedure. (a) A monochromatic tunable laser illuminates a MMF. The output field at different axial positions is captured as images on a CCD camera. A reflective phase-only SLM shapes the input wavefront (represented as a transmission one for schematic convenience). (b) For each wavelength, a microscope objective axial scan is performed and a set of images is acquired. (c) Observation of the  $\chi$ -axial effect. A TM is measured at  $\lambda_0 = 800 \text{ nm}$  and  $z_0 = 0$  for a  $50 \mu\text{m}$  core radius fiber of  $58 \text{ mm}$  length. A focusing phase mask is applied on the SLM (central panel). The focus remains varying both the wavelength and the axial position. (d) Correlation plot of speckles acquired for the same fiber as in (c). A high-valued antidiagonal correlation region is visible. Color dots make the correspondence with the images of (c). Profile widths along  $z(l_z)$  and  $\lambda(l_\lambda)$  axes are presented on the side.

addition, these plots illustrate that the  $\chi$ -axial ME extends over limited spectral and axial ranges and that the longer the fiber, the steeper the correlation slope [Fig. 2(a)]. Notably, the spectral and axial correlation ranges associated with the  $\chi$ -axial coupling are both larger than the ones usually defined for fixed  $\lambda$  (Rayleigh length:  $l_z = \frac{2\lambda}{NA^2}$ <sup>32</sup>) and  $z$  ( $l_\lambda = \frac{2n_1\lambda^2}{LNA^2}$ <sup>7,33</sup>).  $l_z$  and  $l_\lambda$  are illustrated in Fig. 1(d), and their experimental values are given in the supplementary material. We thus now present a simple model allowing us to discuss how the correlation slope scales with physical parameters in the ray optics approximation.

### B. Interpretation of the $\chi$ -axial ME in the framework of the ray optics approximation

Since the fiber diameters (50 and 105  $\mu\text{m}$ ) are large in comparison to the working wavelength  $\lambda_0 = 800$  nm, supporting, respectively, around 500 and 2000 transverse modes per polarization, we first consider a ray optics approximation model.<sup>34</sup> In a SI-fiber, the modulus of the transverse component of the wavevector is conserved and the optical path length along a multiple bouncing trajectory scales quadratically with the incident angle,<sup>26</sup> similar to the phase accumulated under free-space propagation in the Fresnel approximation. The Fresnel diffraction formula implies that the intensity is unchanged when the product  $\lambda z$ , appearing as the prefactor of the quadratic phase, is conserved, thereby resulting in the  $\chi$ -axial effect.<sup>28</sup> In a SI-MMF, taking the differential of the equation  $\lambda z = \text{const.}$  results in the following slope for the  $\chi$ -axial ME at the fiber output:

$$\frac{\delta z}{\delta \lambda} = -\frac{L}{n_1 \lambda_0}, \quad (2)$$

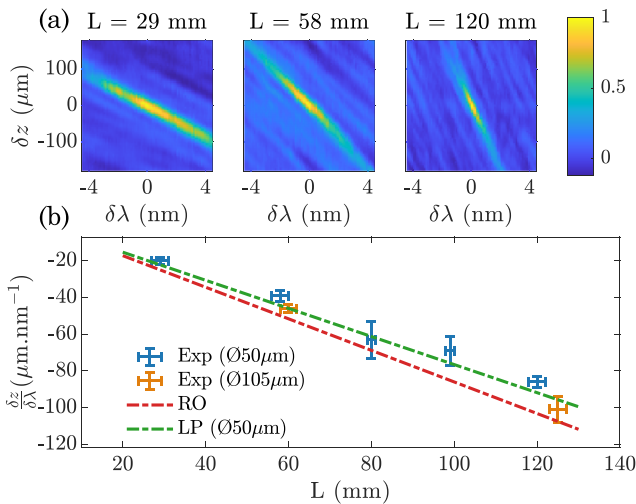


**FIG. 2.** (a) Correlations in the  $(\delta z, \delta \lambda)$  plane plotted for three fiber lengths: 29, 56, and 120 mm. The observed effect is present in all three cases, but its slope  $(\delta z/\delta \lambda)$  depends on the fiber length. (b) Experimental slopes measured for different fiber lengths and two core diameters  $\text{Ø} = 50 \mu\text{m}$  (blue dots) and  $\text{Ø} = 105 \mu\text{m}$  (orange dots). The expected slope obtained from ray optics (RO) calculations is represented with the red dashed line. The green dashed line represents the slope obtained from the calculation with the linearly polarized (LP) modes (for  $\text{Ø} = 50 \mu\text{m}$  and  $\epsilon = 0.11$  [see Eq. (8)]). Error bars are obtained from 95% confidence bounds of the slope extraction and fiber length measurement.

where  $L$  is the fiber length and  $n_1$ , the refractive index contrast of the core with the output medium, is due to Snell–Descartes’s law applying at the output facet of the MMF [see the supplementary material for the derivation of Eq. (2)]. A spectral shift of the impinging beam thus results in a homothetic axial dilation of the intensity in the SI-MMF, with the origin of the homothety at the input facet of the fiber. This is noticeably different from the  $\chi$ -axial ME in forward scattering slabs<sup>27</sup> wherein the origin of the dilation was found to be in a virtual plane located at 1/3 of the slab thickness.<sup>28,29</sup> Here, multiple scattering events lead to a random walk in k-space that shifts the origin of the dilation. The slope obtained from Eq. (2) is plotted in Fig. 2(b), showing good agreement with the corresponding experimental measurements. Notably, within the framework of the ray optics model, the slope does not depend on the fiber radius, which is in qualitative agreement with experimental observations for the 50  $\mu\text{m}$  and 105  $\mu\text{m}$  fibers that exhibit similar slopes, since this model is justified in both cases. However, although the ray model well predicts the measured slopes, it does not explain why the effect remains limited to finite  $\chi$ -axial ranges, as observed experimentally [Figs. 1(d) and 2(a)]. A wave model is required to understand and estimate the observed limited spectral correlation width  $\Delta \lambda$  and the limited axial range scanning ability  $\Delta z$ . In the following, we thus propose to analyze our results in the framework of the SI-MMF eigenmodes, assuming cylindrical symmetry for the fibers.

### III. EXPERIMENTAL AND THEORETICAL COMPARISON OF THE $\chi$ -AXIAL ME IN THE FRAMEWORK OF LP MODES

#### A. Correlation between the spectral and the axial shifts

Here, we express the fiber modes in terms of linearly polarized (LP) modes to calculate an analytical expression for the cross-correlation product [Eq. (1)] as a function of  $z$  and  $\delta \lambda$ . The slope of the  $\chi$ -axial effect and its spectral and axial bandwidths arise from this expression. Importantly, all calculations are carried out inside the fiber and do not consider free-space propagation outside, making these results not specific to our experimental system but revealing the intrinsic spectro-axial properties of SI-MMF. In addition, for the sake of simplicity of expressions, spectral components of the field are now described by their angular frequencies  $\omega = 2\pi c/\lambda$ , with  $c$  being the light speed in vacuum, rather than by their wavelength  $\lambda$ .

SI-MMF propagation eigenmodes are, in the weak guidance approximation, LP modes.<sup>35</sup> The field propagating in a fiber of radius  $a$  can then be expressed as

$$E_\omega(\mathbf{r}, z) = \sum_{l,m} \tilde{E}_{l,m}(\omega) e^{i\beta_{l,m}z} e^{il\varphi} J_l\left(u_{l,m} \frac{r}{a}\right), \quad (3)$$

where  $a$  is the fiber radius,  $l$  and  $m$  are the azimuthal and radial numbers of the LP modes, respectively,  $J_l$  is the Bessel function of the first kind of order  $l$ , and  $\beta_{l,m}$  and  $u_{l,m}$ , the longitudinal and transverse wavenumbers, respectively, are imposed by continuity equations at the core–cladding boundary.

Assuming that the fields in the fiber are random patterns with Gaussian statistics,<sup>36</sup> the cross-correlation product of Eq. (1) is

$$C(\omega, \omega', z, z') \propto |\langle E_\omega E_{\omega'}^* \rangle|^2, \quad (4)$$

up to a normalization factor. As discussed in the [supplementary material](#), intensity correlations at the fiber output are dominated by the phase delays accumulated along the fiber due to the chromatic dependence of  $\beta_{l,m}$ ,

$$C(\omega, \omega', z, z') = \left| \left\langle e^{i[\beta_{l,m}(\omega)z - \beta'_{l,m}(\omega')z']} \right\rangle_{l,m} \right|^2, \quad (5)$$

where, assuming ergodic hypothesis, statistical averaging is replaced by modal averaging over  $l$  and  $m$  values. Equation (5) appears as the characteristic function of variables  $\delta[\beta_{l,m}(\omega)z - \beta'_{l,m}(\omega')z']$ , which we approximate to the normal one, hence giving

$$C(\omega, \omega', z, z') \simeq \exp(-\text{Var}\{\delta[\beta_{l,m}(\omega)z]\}), \quad (6)$$

where the variance is calculated over all possible  $l$  and  $m$  values. The axial shift  $\delta z$  that maximizes the correlation coefficient (i.e., minimizes the variance) for a given spectral shift  $\delta\omega$  is thus an extremum of  $C$  obtained by solving

$$\frac{\partial}{\partial(\delta z)} \text{Var}[\delta(\beta_{l,m}z)] = 0, \quad (7)$$

leading to (see the [supplementary material](#))

$$\delta z = (1 - \epsilon) \frac{z}{\omega} \delta\omega, \quad (8)$$

where  $\epsilon$  is a positive constant scaling as  $1/v$ , with  $v = \omega a \text{NA}/c$ , the normalized frequency. For large fiber cores ( $\omega a/c \gg 1$ ),  $\epsilon$  vanishes. Numerical simulation further reveals that the product  $v\epsilon$  does not strongly depend either on the NA or on the core diameter. On average,  $v\epsilon$  is found to be numerically on the order of 4.7 for both  $50 \mu\text{m}$  and  $105 \mu\text{m}$  core diameters (see the [supplementary material](#)).

In the large core limit, Eq. (8) leads to Eq. (2) obtained in the ray optic model. The axial shift analytically found in Eq. (8) in the frame

of LP-mode modeling is compared to the ones obtained experimentally and theoretically in the ray optics framework in Fig. 2(b). To compare Eq. (8) to the experimental data, the slope value in Eq. (8) is divided by  $n_1$  to take into account the Snell–Descartes relation when exiting the fiber.

### B. Spectral and axial widths of the ME

We now consider the observed correlation width of the  $\chi$ -axial ME along the correlation line [Fig. 2(a)]. Experimental spectral widths and axial displacement amplitudes are measured at the full width at half maximum (FWHM) by projecting maximal values of the cross-correlation function on the  $\lambda$  and  $z$  axes [see Fig. 3 (top)]. The spectral correlation widths of fibers are observed to depend on their lengths. Conversely, the axial correlation width remains almost unchanged in relation to the fiber length. We measure spectral widths of 7, 3, and 1 nm for the fibers of lengths 29, 58, and 120 mm, respectively, and a mean value of  $130 \mu\text{m}$  for the axial correlation width.

The analytical expression of the correlation width of the  $\chi$ -axial ME along the correlation line may be obtained by plugging Eq. (8) into the expression of the correlation function Eq. (6). Replacing  $\delta z$  by  $\delta\omega$  in Eq. (6) according to Eq. (8), we get

$$\max_{\delta z} C = \exp\left[-\left(\frac{\delta\omega}{\Delta\omega}\right)^2\right], \quad (9)$$

with

$$\Delta\omega = \alpha \frac{2n_1 \omega a}{\text{NA}z}, \quad (10)$$

where  $\alpha$  is a prefactor close to one on average and whose exact value is discussed in the [supplementary material](#). The spectral width results are presented in Fig. 3(a) (bottom), where we plotted together the analytical formula Eq. (9) (dashed lines) and the results of

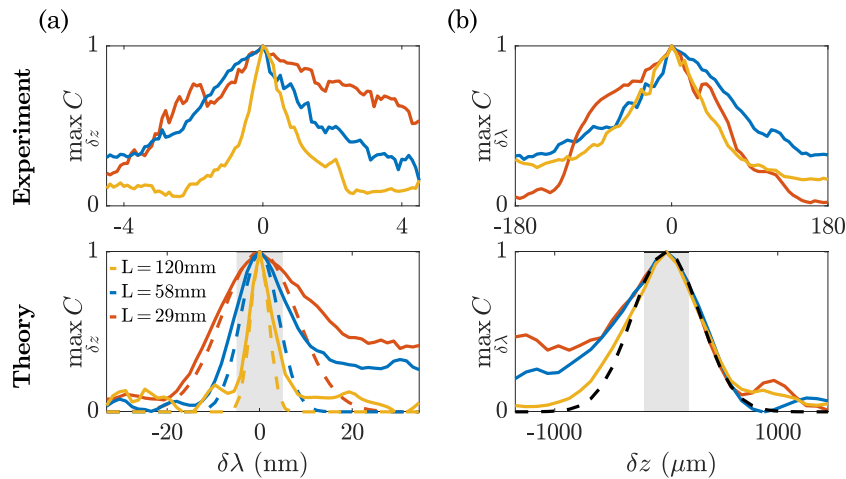


**FIG. 3.** Ranges of the  $\chi$ -axial ME. The top graphs represent experimental correlation plots projected on the  $\lambda$  (respectively,  $z$ ) axis. Different fibers (of  $50 \mu\text{m}$  diameter) are distinguished by line colors: red for  $L = 29$  mm, blue for  $58$  mm, and yellow for  $120$  mm. The bottom graph displays fiber intrinsic spectral and axial widths (solid lines) and their comparison to the theoretical values obtained from the LP model (dashed lines) for the same three fiber lengths. (a) Spectral width varies with the fiber length. The bottom gray domains indicate where the top corresponding experimental data are measured, showing a scale factor of 5. (b) Axial width: because it does not depend on the fiber length, only one plot (black dashed line) is presented for the analytical model.

numerical simulations (solid lines). As expected and experimentally observed, the spectral width depends on the fiber length. From the analytical LP model, we calculate expected spectral widths of 20, 10, and 5 nm for fibers of lengths 29, 58, and 120 mm, respectively. These theoretical values are larger than the experimental ones by a factor  $\sim 3$  for the shortest fiber and up to 5 for the longest fiber, but both the orders of magnitude and the global evolution trend with fiber lengths agree.

Making use of Eq. (8), the correlation product can also be expressed as a function of the axial shift as

$$\max_{\delta\omega} C = \exp\left[-\left(\frac{\delta z}{\Delta z}\right)^2\right], \quad (11)$$

with the axial correlation range

$$\Delta z = \alpha(1 - \epsilon) \frac{2n_1 a}{\text{NA}}, \quad (12)$$

which, in agreement with experimental observations, does not depend on the fiber length. The simulated axial width and the Gaussian analytical prediction are shown in Fig. 3(b) (bottom). The axial correlation range obtained with the LP model is  $700 \mu\text{m}$  inside the fiber, yielding  $480 \mu\text{m}$  outside the fiber, once the Snell–Descartes law is taken into account. As for the spectral correlation width, the theoretical value is a factor 3 above than the one obtained experimentally ( $130 \mu\text{m}$ ). In Fig. 3, it appears that the theoretical model agrees with the numerical simulations, except for the largest values of  $\delta\lambda$  and the smallest values of  $\delta z$ . We attribute this discrepancy to the limit of validity of our modeling hypothesis. Moreover, our model solely addresses the case of perfect fibers, thus ignoring modal couplings in the fiber and fibers face imperfections, which are unavoidable for real fibers.

#### IV. DISCUSSION

A detailed analysis of the contribution of the different modes to the total  $\chi$ -axial ME presented in the [supplementary material](#) reveals the key role of the less confined modes. Our model assumes that the transverse profiles of LP modes are achromatic, but this approximation becomes inaccurate when the spectral correlation width is very large, as implied for short fibers, hence the better matching of the model with numerical simulations for the longest fiber than for the shortest one in Fig. 3. The spectral sensitivity of the less confined modes also suggests that it is possible to broaden the spectral correlation width of the  $\chi$ -axial ME by limiting the light coupling to the lowest NA modes or by filtering high-NA modes at the output (i.e., working at a numerical aperture slightly below the one of the fiber, still allowing high-resolution imaging if an in-purpose higher-NA fiber is used). Another way to improve the results could be to better fulfill the achromatic input field hypothesis by imaging the SLM in the fiber proximal end instead of imaging it on the microscope objective back aperture.

Finally, for applications where the  $\chi$ -axial ME is of interest after exiting the fiber, the intrinsic correlation width of the fiber is not the only limitation to consider: a mere geometric limitation arises. Indeed, when imaging planes far away, outside the fiber emission cone (defined by the fiber radius and its numerical aperture), the maximum spatial frequency decreases resulting in larger patterns

that no-longer correlate with fields near the fiber output facet. This geometrical effect thus limits the axial scan to  $\delta z_c = \frac{2a}{\text{NA}} \simeq 230 \mu\text{m}$  that translates into a spectral width limitation adding to the intrinsic correlation range of the fiber. Importantly, for practical applications, both limitations are of the same order of magnitude: the FWHM of the intrinsic LP axial width is [using Eq. (11)]  $2 \ln(2) \Delta z \simeq 2.5 \delta z_c$ . None of the mentioned phenomena should then dominate.

#### V. CONCLUSION

In conclusion, we experimentally demonstrated and quantified the  $\chi$ -axial ME in a SI-MMF. Two different theoretical approaches enable us to predict the value of the  $\chi$ -axial shift. A simple ray optics model gives access to the shift only using easily accessible fiber parameters with a good degree of approximation. However, in the frame of this model, an infinite spectral width is predicted and slight discrepancies arise on the slope of the  $\chi$ -axial ME when the field penetration inside the fiber cladding cannot be neglected. The framework of LP modes not only brings more accuracy on the slope of the  $\chi$ -axial ME but also allows the derivation of its correlation width. We observe that the studied  $\chi$ -axial scanning ranges are not infinite and also obtain that it is possible to optimize the effect: analytical results demonstrate that working with the most confined modes would allow extending significantly the spectro-axial correlation range of this ME. For imaging purposes, when a large spectral bandwidth is required, working with short MMF should be preferred. Alternatively, avoiding the excitation of the less confined modes is expected to increase the spectral correlation range, in principle, up to arbitrarily large values.

Characterization of the  $\chi$ -axial ME in MMFs is of high importance to simplify light-beam manipulation by using the blind control of polychromatic wavefields at distal facets, especially for imaging applications. Thanks to the  $\chi$ -axial ME, only one TM measurement would be needed to perform foci on different  $z$  planes and thereby overcome the current inability of wavelength tuning while imaging.<sup>30</sup> Furthermore, the  $\chi$ -axial ME knowledge enables *a priori* wavefront correction to achieve non-linear microscopy<sup>37,38</sup> and to extend the confocal microscopy technique of Ref. 39 for objects subjected to inelastic scattering or broadband fluorescence. This fast axial scan ability opens up the possibility of extending the “spot scanning” imaging technique in three dimensions,<sup>13,40</sup> paving the way to non-invasive imaging (in biological media, for instance).

#### SUPPLEMENTARY MATERIAL

See the [supplementary material](#) for information on the devices and experimental precautions, the derivation of the analytical model for ray optics and LP modes as well as the LP modes simulations details, and a discussion of the role of the less confined modes.

#### ACKNOWLEDGMENTS

We thank Michał Dąbrowski and Lorenzo Valzania for careful reading of the manuscript and fruitful comments. This project was funded by the European Research Council [Grant Agreement No. 724473 (SMARTIES)]. S.G. and M.G. are members of the Institut Universitaire de France.

## AUTHOR DECLARATIONS

## Conflict of Interest

The authors have no conflicts to disclose.

## DATA AVAILABILITY

The data that support the findings of this study are available from the corresponding author upon reasonable request.

## REFERENCES

- <sup>1</sup>D. J. Richardson, J. M. Fini, and L. E. Nelson, "Space-division multiplexing in optical fibres," *Nat. Photonics* **7**, 354–362 (2013).
- <sup>2</sup>L. G. Wright, D. N. Christodoulides, and F. W. Wise, "Spatiotemporal mode-locking in multimode fiber lasers," *Science* **358**, 94–97 (2017).
- <sup>3</sup>T. Steinmetz, Y. Colombe, D. Hunger, T. W. Hänsch, A. Balocchi, R. J. Warburton, and J. Reichel, "Stable fiber-based Fabry-Pérot cavity," *Appl. Phys. Lett.* **89**, 111110 (2006).
- <sup>4</sup>S. Leedumrongwatthanakun, L. Innocenti, H. Defienne, T. Juffmann, A. Ferraro, M. Paternostro, and S. Gigan, "Programmable linear quantum networks with a multimode fibre," *Nat. Photonics* **14**, 139–142 (2020).
- <sup>5</sup>M. W. Matthès, P. del Hougne, J. de Rosny, G. Lerosey, and S. M. Popoff, "Optical complex media as universal reconfigurable linear operators," *Optica* **6**, 465–472 (2019).
- <sup>6</sup>B. Redding, M. Alam, M. Seifert, and H. Cao, "High-resolution and broadband all-fiber spectrometers," *Optica* **1**, 175–180 (2014).
- <sup>7</sup>B. Redding, S. M. Popoff, and H. Cao, "All-fiber spectrometer based on speckle pattern reconstruction," *Opt. Express* **21**, 6584–6600 (2013).
- <sup>8</sup>Y. Choi, C. Yoon, M. Kim, T. D. Yang, C. Fang-Yen, R. R. Dasari, K. J. Lee, and W. Choi, "Scanner-free and wide-field endoscopic imaging by using a single multimode optical fiber," *Phys. Rev. Lett.* **109**, 203901 (2012).
- <sup>9</sup>I. N. Papadopoulos, S. Farahi, C. Moser, and D. Psaltis, "High-resolution, lensless endoscope based on digital scanning through a multimode optical fiber," *Biomed. Opt. Express* **4**, 260–270 (2013).
- <sup>10</sup>F. Roddier, *Adaptive Optics in Astronomy* (Cambridge University Press, 1999).
- <sup>11</sup>R. K. Tyson, *Principles of Adaptive Optics* (CRC Press, 2015).
- <sup>12</sup>S. M. Popoff, G. Lerosey, R. Carminati, M. Fink, A. C. Boccarda, and S. Gigan, "Measuring the transmission matrix in optics: An approach to the study and control of light propagation in disordered media," *Phys. Rev. Lett.* **104**, 100601 (2010).
- <sup>13</sup>I. N. Papadopoulos, S. Farahi, C. Moser, and D. Psaltis, "Focusing and scanning light through a multimode optical fiber using digital phase conjugation," *Opt. Express* **20**, 10583–10590 (2012).
- <sup>14</sup>J. W. Goodman, "Some fundamental properties of speckle," *J. Opt. Soc. Am.* **66**, 1145 (1976).
- <sup>15</sup>R. Di Leonardo and S. Bianchi, "Hologram transmission through multi-mode optical fibers," *Opt. Express* **19**, 247–254 (2011).
- <sup>16</sup>T. Čižmar and K. Dholakia, "Exploiting multimode waveguides for pure fibre-based imaging," *Nat. Commun.* **3**, 1027 (2012).
- <sup>17</sup>M. Plöschner, T. Tyc, and T. Čižmar, "Seeing through chaos in multimode fibres," *Nat. Photonics* **9**, 529–535 (2015).
- <sup>18</sup>M. W. Matthès, Y. Bromberg, J. de Rosny, and S. M. Popoff, "Learning and avoiding disorder in multimode fibers," *Phys. Rev. X* **11**, 021060 (2021).
- <sup>19</sup>A. M. Caravaca-Aguirre, E. Niv, D. B. Conkey, and R. Piestun, "Real-time resilient focusing through a bending multimode fiber," *Opt. Express* **21**, 12881–12887 (2013).
- <sup>20</sup>S. Li, C. Saunders, D. J. Lum, J. Murray-Bruce, V. K. Goyal, T. Cizmar, and D. B. Phillips, "Compressively sampling the optical transmission matrix of a multimode fibre," *Light: Sci. Appl.* **10**(1), 1–15 (2021).
- <sup>21</sup>S. Feng, C. Kane, P. A. Lee, and A. D. Stone, "Correlations and fluctuations of coherent wave transmission through disordered media," *Phys. Rev. Lett.* **61**, 834–837 (1988).
- <sup>22</sup>I. Freund, M. Rosenbluh, and S. Feng, "Memory effects in propagation of optical waves through disordered media," *Phys. Rev. Lett.* **61**, 2328–2331 (1988).
- <sup>23</sup>B. Judkewitz, R. Horstmeyer, I. M. Vellekoop, I. N. Papadopoulos, and C. Yang, "Translation correlations in anisotropically scattering media," *Nat. Phys.* **11**, 684–689 (2015); [arXiv:1411.7157](https://arxiv.org/abs/1411.7157).
- <sup>24</sup>G. Osnabrugge, R. Horstmeyer, I. N. Papadopoulos, B. Judkewitz, and I. M. Vellekoop, "Generalized optical memory effect," *Optica* **4**, 886 (2017).
- <sup>25</sup>L. V. Amitonova, A. P. Mosk, and P. W. H. Pinkse, "Rotational memory effect of a multimode fiber," *Opt. Express* **23**, 20569 (2015).
- <sup>26</sup>S. Li, S. A. Horsley, T. Tyc, T. Čižmar, and D. B. Phillips, "Memory effect assisted imaging through multimode optical fibres," *Nat. Commun.* **12**, 3751 (2021).
- <sup>27</sup>A. G. Vesga, M. Hofer, N. K. Balla, H. B. De Aguiar, M. Guillon, and S. Brasselet, "Focusing large spectral bandwidths through scattering media," *Opt. Express* **27**, 28384–28394 (2019).
- <sup>28</sup>L. Zhu, J. Boutet de Monvel, P. Berto, S. Brasselet, S. Gigan, and M. Guillon, "Chromato-axial memory effect through a forward-scattering slab," *Optica* **7**, 338–345 (2020).
- <sup>29</sup>P. Arjmand, O. Katz, S. Gigan, and M. Guillon, "Three-dimensional broadband light beam manipulation in forward scattering samples," *Opt. Express* **29**, 6563–6581 (2021).
- <sup>30</sup>T. Pikálek, J. Trägårdh, S. Simpson, and T. Čižmar, "Wavelength dependent characterization of a multimode fibre endoscope," *Opt. Express* **27**, 28239–28253 (2019).
- <sup>31</sup>R. Turcotte, C. C. Schmidt, M. J. Booth, and N. J. Emptage, "Volumetric two-photon fluorescence imaging of live neurons using a multimode optical fiber," *Opt. Lett.* **45**, 6599–6602 (2020).
- <sup>32</sup>C. Halford, W. Gamble, and N. George, "Experimental investigation of the longitudinal characteristics experimental investigation of the longitudinal characteristics of laser speckle," *Opt. Eng.* **26**, 261263 (1987).
- <sup>33</sup>E. G. Rawson, J. W. Goodman, and R. E. Norton, "Frequency dependence of modal noise in multimode optical fibers," *J. Opt. Soc. Am.* **70**, 968–976 (1980).
- <sup>34</sup>J. D. Jackson, *Classical Electrodynamics*, 3rd ed. (John Wiley & Sons, 1999).
- <sup>35</sup>A. W. Snyder and J. Love, *Optical Waveguide Theory* (Springer Science & Business Media, 2012).
- <sup>36</sup>I. Reed, "On a moment theorem for complex Gaussian processes," *IRE Trans. Inf. Theory* **8**, 194–195 (1962).
- <sup>37</sup>E. E. Morales-Delgado, D. Psaltis, and C. Moser, "Two-photon imaging through a multimode fiber," *Opt. Express* **23**, 32158–32170 (2015).
- <sup>38</sup>M. Hofer, S. Shivkumar, B. El Waly, and S. Brasselet, "Coherent anti-Stokes Raman scattering through thick biological tissues by single-wavefront shaping," *Phys. Rev. Appl.* **14**, 024019 (2020).
- <sup>39</sup>D. Loterie, S. A. Goorden, D. Psaltis, and C. Moser, "Confocal microscopy through a multimode fiber using optical correlation," *Opt. Lett.* **40**, 5754–5757 (2015).
- <sup>40</sup>N. Stasio, D. B. Conkey, C. Moser, and D. Psaltis, "Light control in a multicore fiber using the memory effect," *Opt. Express* **23**, 30532–30544 (2015).